physics

MDPI

Article

Dynamical Correlations and Chimera-like States of Nanoemitters Coupled to Plasmon Polaritons in a Lattice of Conducting Nanorings

Boris A. Malomed [1,2], Gennadiy Burlak [3,*], Gustavo Medina-Ángel [3,4] and Yuri Karlovich [5]

[1] Department of Physical Electronics, School of Electrical Engineering, Faculty of Engineering, Center for Light-Matter Interaction, Tel Aviv University, Tel Aviv P.O. Box 39040, Israel; malomed@tauex.tau.ac.il
[2] Instituto de Alta Investigación, Universidad de Tarapacá, Casilla 7D, Arica 1000000, Chile
[3] Centro de Investigación en Ingeniería y Ciencias Aplicadas, Universidad Autónoma del Estado de Morelos, Av. Universidad 1001, Cuernavaca 62209, Morelos, Mexico; gustavo.medina@alumnos.uaem.mx
[4] Facultad de Contaduría, Administración e Informática, Universidad Autónoma del Estado de Morelos, Av. Universidad 1001, Cuernavaca 62209, Morelos, Mexico
[5] Centro de Investigación en Ciencias, Universidad Autónoma del Estado de Morelos, Av. Universidad 1001, Cuernavaca 62209, Morelos, Mexico; karlovich@uaem.mx
* Correspondence: gburlak@uaem.mx

Abstract

We systematically investigate semiclassical dynamics of the optical field produced by quantum nanoemitters (NEs) embedded in a periodic lattice of conducting nanorings (NRs), in which plasmon polaritons (PPs) are excited. The coupling between PPs and NEs through the radiated optical field leads to establishment of a significant cross-correlation between NEs, so that their internal dynamics (photocurrent affected by the laser irradiation) depends on the NR's plasma frequency ω_p. The transition to this regime, combined with the nonlinearity of the system, leads to a quite increase in the photocurrent in the NEs, as well as to non-smooth (chimera-like or chaotic) behavior in the critical (transition) region, where considerably small variations in ω_p lead to significant changes in the level of the NE pairwise cross-correlations. The chimera-like state is realized as coexistence of locally synchronized and desynchronized NE dynamical states. A fit of the dependence of the critical current on ω_p is found, being in agreement with results of numerical simulations. The critical effect may help to design new optical devices, using dispersive nanolattices which are made available by modern nanoelectronics.

Keywords: semiclassical dynamics; quantum nanoemitters; conducting nanorings; plasmon polaritons; cross-correlation; chimera-like state; finite-difference time-domain (FDTD) numerical method

Check for updates

Received: 21 November 2025
Revised: 30 December 2025
Accepted: 8 January 2026
Published: 16 February 2026

Copyright: © 2026 by the authors. Licensee MDPI, Basel, Switzerland. This article is an open access article distributed under the terms and conditions of the Creative Commons Attribution (CC BY) license.

1. Introduction

The current work in the field of infrared photoelectric information technologies yields advances in the generation, manipulation, source detection, and related achievements in the field of infrared photonics [1–6]. The inclusion of dispersive nanorings (NRs) in the operation of nanoemitters (NEs) considerably affects the generated electromagnetic field, whose structure significantly depends on the NR's plasma frequency ω_p [7,8]. In such hybrid systems, it is possible to control properties of local optical fields and the creation of miniaturized low-threshold coherent tunable sources [8,9]. An essential feature of these structures in the disordered state is that NE clusters produce fractal radiation patterns, in

which light is simultaneously emitted and scattered [10]. In the practically relevant case of lossy NRs with embedded NEs, other factors become significant too. Optical fields of dispersive NRs perturb the energy levels of NEs; hence, plasmon polaritons (PPs) populating NRs affect the internal degrees of freedom of the quantum NEs coupled to the NRs. Nonlinearity is a significant feature of NEs, which leads to laser emission [11]. All that leads to resonant changes in the field structure associated with the PP excitation in the NRs. It was found that such a system exhibits coexistence of locally synchronized and desynchronized dynamics of random NEs, which may be considered as a chimera-like behavior in the respective range of ω_p. We remind that a "chimera state" is a dynamical pattern that occurs in a network of coupled identical oscillators when the oscillator population is broken into synchronous and asynchronous parts [12,13]. The PP field being external to the field in the NEs, at considerably small values of ω_p the NE dynamics are practically independent of ω_p. However, at overcritical values of ω_p, i.e., above the transition to the state with the strong coupling of the NR and NE subsystems, the NE photocurrent essentially depends on ω_p.

In this paper, we theoretically study dynamics and correlations of quantum NEs embedded in a periodic lattice of conducting NRs, in which the PPs are excited. We show that the coupling between PPs and NEs through the optical field leads to a significant correlation between NEs, so that the internal dynamics of the NEs (quantum photocurrent) depends on the plasma frequency ω_p of the classical subsystem of PPs in the NR. Thus, the setup is built of two subsystems coupled by the radiation field, viz., the classical array of the NRs and the quantum (actually, semi-classical) subsystem of NEs. We consider conducting (carbon) NRs, whose properties are determined by ω_p. The PP field interacts with NEs and perturbs its quantum degrees of freedom. We show that the field dynamics are distinct in different ranges of ω_p, which can be separated by some characteristic value ω_c. At considerably small $\omega_p < \omega_c$, the PP field has a considerably small amplitude, weakly enough perturbing the quantum dynamics and securing smooth cross-correlations of the NEs. However, at larger $\omega_p \geq \omega_c$, a transition occurs to the state in which the PP field produces a significant contribution to the radiation, which perturbs the dynamics of NEs, leading to a change in their cross-correlations.

The rest of the paper is organized as follows. In Section 2, we formulate basic equations for the considered hybrid NR-NE coupled system. In Section 3, we study dispersion characteristics and the field structure of the plasmonic modes in the NRs. In Section 4, we investigate the structure of the optical field of the laser emission in the system and the PP-mediated dynamics of the NEs coupled to NRs. In Section 5, we explore the phase transition exhibited by the total PP current in the lattice. Section 6 concludes the paper.

2. Basic Equations

The quantum system under consideration in Figure 1 contains a periodic two-dimensional (2D) lattice of conducting NRs (7×7) with a randomly embedded rarefied set of quantum NEs (only four in Figure 1, shown by solid circles) emitting the optical field. PPs are excited in the NRs and interact with the embedded NEs through the radiation field.

In Figure 1 the NEs are connected by straight lines corresponding to the optimized path calculated using the TSP (traveling salesman problem) technique and Fermat's principle [14]. In such a configuration, the length of the connecting path A_D (see Figure 1) is proportional to the optimized (dimensionless) distance, which is a number of nodes in the numerical grid, which a photon can travel in the sample, passing each NE without visiting the same NE twice. Accordingly, A_D is calculated in the framework of our numerical analysis by dint of the TSP (traveling salesman problem) technique [10,14]. The color scheme indicates that the embedded NEs in Figure 1 consist of two clusters. To study this hybrid

system, we use time-dependent Maxwell's equations in the lattice of 2D NRs, coupled to the semi-classical rate equations for the electron populations in the NE [11].

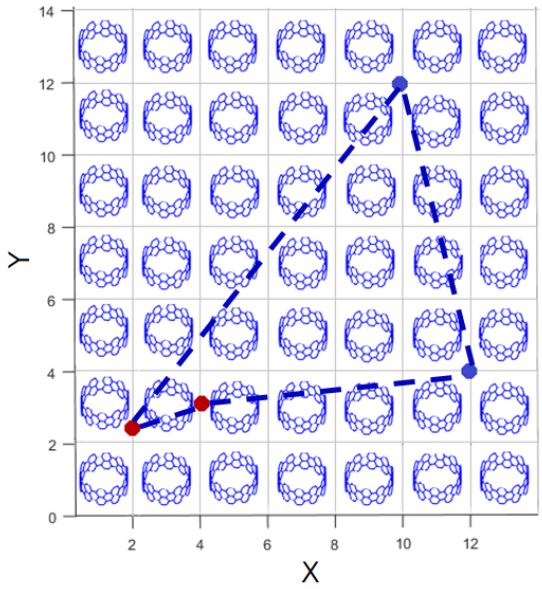


Figure 1. The system built as the 7×7 2D lattice (dimensionless axis X, Y), composed of conducting nanorings (NRs) with embedded quantum nanoemitters (NEs), which emit the optical field (solid circles). Numbers attached to the horizontal and vertical axes refer to coordinates of lattice cells. Each cell contains a single NR, and the numeration of the cells is aligned with centers of the NRs. In the present setup, four NEs form two clusters, as indicated by red and blue circles, respectively. Plasmon polaritons (PPs) are excited in the NRs and interact with the NEs. The NEs are connected by dashed blue straight lines that correspond to the optimized path A_D calculated by means of the TSP (traveling salesman problem) method (so that a traveling photon passes each NE, without visiting the same NE twice) and the Fermat's principle [10,14].

The Maxwell equations are [14,15]

$$\nabla \times \mathbf{E} = -\mu_0 \frac{\partial \mathbf{H}}{\partial t}, \nabla \times \mathbf{H} = \varepsilon_0 \frac{\partial \mathbf{E}}{\partial t} + \mathbf{J} + \frac{\partial \mathbf{P}}{\partial t}, \tag{1}$$

where t denotes the time, $\mathbf{E}$ and $\mathbf{B}$ denote, respectively, the electric and magnetic fields, μ_0 and ε_0 are, respectively, the permeability and permittivity in the vacuum, $\mathbf{J} = \sum_k \mathbf{J}_k(\mathbf{R}_k^{\mathrm{NR}}, t)\delta_{\mathbf{r}\mathbf{R}_k^{\mathrm{NR}}}$ is the PP electrical current in the NRs placed at spatial positions $\mathbf{R}_k^{\mathrm{NR}}$, and $\mathbf{P} = \sum_k \mathbf{P}_k(\mathbf{R}_k^{\mathrm{NE}}, t)\delta_{\mathbf{r}\mathbf{R}_k^{\mathrm{NE}}}$ is the electron polarization in the embedded NE placed at $\mathbf{R}_k^{\mathrm{NE}}$ and $\mathbf{r}$ denotes $3D$ space. Here, N_r and N_s are the number of NRs and NEs respectively, $\delta_{\mathbf{r}\mathbf{R}}$ is Kronecker's symbol, and the sums run over all NRs ($k = 1, N_r$) and NEs ($k = 1, N_s$). In Equation (1), the electric current of the conducting electrons in the NRs obeys the material equation [16] $\dot{\mathbf{J}}_k + \gamma_e \mathbf{J}_k = \varepsilon_0 \omega_p^2 \mathbf{E}$, where γ_e is the collision frequency of electrons and the dot on top denotes the time derivative.

In the semi-classical approximation for non-interacting electrons, the evolution equation for $\mathbf{P}_k$ in the vicinity of the embedded NE is [11]

$$\frac{\partial^2 \mathbf{P}_k}{\partial t^2} + \Delta\omega_a \frac{\partial \mathbf{P}_k}{\partial t} + \omega_a^2 \mathbf{P}_k = \frac{6\pi\varepsilon_0 c^3}{\tau_{21}\omega_a^2}(N_{1,k} - N_{2,k})\mathbf{E}_k, \tag{2}$$

where c is the speed of light in the vacuum.

To complete the model, we add the rate equations [11] for the occupation numbers of NEs, $N_{i,k} = N_i(\mathbf{R}_k^{\mathrm{NE}}, t)$ (following ref. [15], we assume that the NEs are four-level quantum dots, as illustrated by Figure 2):

$$\frac{\partial N_{0,k}}{\partial t} = -A_r N_{0,k} + \frac{N_{1,k}}{\tau_{13}}, \quad \frac{\partial N_{3,k}}{\partial t} = A_r N_{0,k} - \frac{N_{3,k}}{\tau_{02}}, \tag{3}$$

$$\frac{\partial N_{1,k}}{\partial t} = \frac{N_{2,k}}{\tau_{32}} - M_k - \frac{N_{1,k}}{\tau_{13}}, \quad \frac{\partial N_{2,k}}{\partial t} = \frac{N_{1,k}}{\tau_{12}} + M_k - \frac{N_{2,k}}{\tau_{02}}, \tag{4}$$

$$M_k = \frac{(\mathbf{I}_\mathbf{p} \cdot \mathbf{E})_k}{\hbar \omega_a}, \mathbf{I}_{\mathbf{p}k} = \frac{\partial \mathbf{P}_k}{\partial t}, \tag{5}$$

with $\hbar$ the reduced Planck constant. Here, $\Delta\omega_a = \tau_{21}^{-1} + 2T_2^{-1}$, where T_2 is the mean time between dephasing events, τ_{21} is the decay time for the spontaneous transition from the second atomic level to the first one, ω_a is the radiation frequency (see, e.g., [11]), and M_k is the induced radiation rate or excitation rate, depending on its sign [15]. Note that components $\mathbf{I}_{pk}$ parallel to $\mathbf{E}_k$ mainly contribute to Equations (4) and (5) [17]. Coefficient A_r is the pump rate for the transition from the ground level (N_0) to the third one (N_3), which is proportional to the pump intensity in the experiment [15].

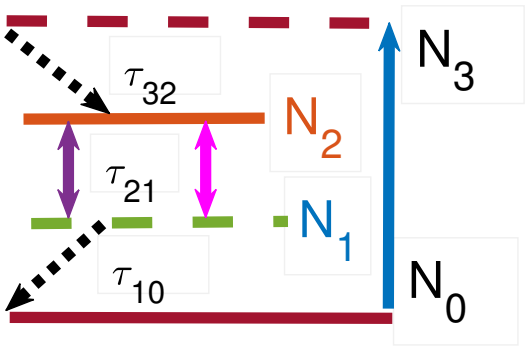


Figure 2. The schematic representation of NE as a four-level system; see Equations (3)–(5). The external pump lifts electrons from the ground level (with population N_0) to the third level (with population N_3). After a short lifetime τ_{32}, the electrons perform the nonradiative transfer to the second level (with population N_2). The second level and the first level (with population N_1) are defined as the upper and lower lasing levels. Electrons are transferred from the upper level to the lower one by both spontaneous and stimulated emission. At last, electrons can perform the nonradiative transfer from the first level back to the ground one.

The finite-difference time-domain (FDTD) numerical method [16] was used to solve the model. In the simulations, we consider the gain medium with parameters of the GaN powder; see [15,18]. In Equations (2)–(4), frequency ω_a is $2\pi\times3\times10^{13}$ Hz, the lifetimes are $\tau_{32} = 0.3$ ps, $\tau_{10} = 1.6$ ps, and $\tau_{21} = 16.6$ ps, and the dephasing time is $T_2 = 0.0218$ ps. In what follows, we use the dimensionless time t normalized as $t \to tc/l_0$, where $l_0 = 100$ μm is the typical spatial scale and c is the light velocity in vacuum. Thus, the present model couples the population-rate equations at different NE levels to the PP field equations in the vicinity of the NR lattice. Therefore, the NE resonant emission operation in the system is affected by the PP excitation in the NRs, which finally leads to essentially nonlinear field dynamics.

Figure 3 shows the temporal dynamics of the PP field distribution in the 7×7 lattice of the conducting NRs (see Figure 1), as produced by our FDTD simulations of Equations (1)–(5) at $\omega_p = 2.3$ THz for different limits t_f of dimensionless simulation times t, such that $t = (0, t_f)$. In Figure 3, the color-coding scheme for the field amplitude shows that, at short times less than 40, the PP field in the NR lattice is small. However, at longer times, an increasingly stronger PP field is generated in the lattice, gradually covering the entire lattice with time.

The local field (designated by the red color) in the vicinity of NEs is quite large, as expected. Figure 3 illustrates the temporal dynamics of the nonlinear transition forming the relationship between the NE oscillators and the PP in the underlying lattice. It shows why the chimera-like states under study (recall they are called chimeras as they combine the synchronized and desynchronized NE dynamical states) depend not only on time, but also on the plasma frequency ω_p of the surrounding NRs.

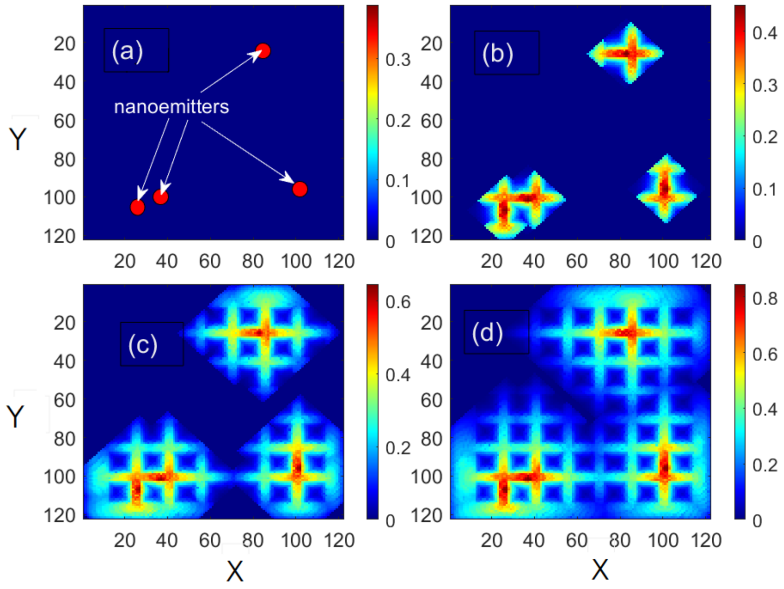


Figure 3. The temporal dynamics (via finite-difference time domin (FDTD) calculations) of spatial distribution of the PP field generated by NEs in the 7×7 lattice of conducting NRs (see Figure 1) for plasma frequency $\omega_p = 2.3$ THz for different simulating times t_f: (**a**) 20, (**b**) 40, (**c**) 60, and (**d**) 80. The color coding represents values of the field amplitude. At long times $t_f > 60$, the PP field, generated in the NR lattice by NEs, gradually covers nearly the entire NR lattice. The local field (shown by the red color) in the vicinity of NEs is the largest (a). The optical field is concentrated in gaps of the NR lattice and practically does not penetrate into the NRs.

3. Plasmon Modes in NRs

The transmission characteristics of surface PPs in ring resonators have been studied in nano-optics under the condition that the frequency dispersion may be neglected [19,20]. However, this approximation is not applicable to the conducting NR in the vicinity of $\omega = \omega_p$. In this Section, we briefly analyze the structure of the spectrum of a single nanoparticle. Below, the optical field in the NR lattice is studied by means of the FDTD technique, see Ref. [16]. As the most fundamental object, we consider a single cylindrical nanoparticle of radius R and L_n, is a length containing N_e valence electrons, assuming that the density of the valence electrons is uniform, $n(\mathbf{r}) \equiv n_0$. The cylindrical geometry admits the propagation of independent transverse magnetic (TM, $[E_\parallel, H_\perp]$) and transverse electric (TE, $[E_\perp, H_\parallel]$) modes with the longitudinal and transverse components of the electric field, the corresponding subscripts being denoted below as $\alpha = \parallel$ and $\perp$ components, respectively. Following Ref. [17], we define the shift $\mathbf{u}_\alpha$ of the electron distribution; hence, one can calculate the respective displaced density as $n(\mathbf{r} - \mathbf{u}_\alpha) \approx n(\mathbf{r}) + \delta n_\alpha$. For considerably small u_α, one has

$$\delta n_\alpha(\mathbf{r}) = -\mathbf{u}_\alpha \cdot \nabla n(\mathbf{r}). \tag{6}$$

The corresponding energy variation is

$$\delta E_\alpha = \frac{e^2}{2} \int \mathrm{d}^3\mathbf{r} \int \mathrm{d}^3\mathbf{r}' \, \frac{\delta n_\alpha(\mathbf{r}) \delta n_\alpha(\mathbf{r}')}{|\mathbf{r} - \mathbf{r}'|}, \tag{7}$$

(with e the elementary charge) and therefore the restoring force is $F_\alpha = -\frac{\partial}{\partial u_\alpha}(\delta E_\alpha) = -k_\alpha u_\alpha$ where k_α is the effective spring constant; hence, the normal mode's frequency is

$$\omega_{0,\alpha} = \sqrt{\frac{k_\alpha}{M_e}}, \tag{8}$$

where $M_e = N_e m_e$ is the full mass of the electrons.

For the longitudinal displacement $\mathbf{u}_{\alpha=\|}$, the variation of the energy in Equation (7) can be written as

$$\delta E_\| = 2\pi^2 (e u n_0)^2 R^3 x[1 - 2y(x)],\ x = L_n/R, \tag{9}$$

where $y(x) = (g(x) - 4/3)/(\pi x)$, and

$$g(x) = \frac{x}{6}\left[\left(x^2+4\right)K\left(-\frac{4}{x^2}\right) - \left(x^2-4\right)E\left(-\frac{4}{x^2}\right)\right], \tag{10}$$

with the complete elliptic integrals of the first (K) and second (E) kinds, respectively [21]:

$$K(x) = \int_0^1 \frac{\mathrm{d}t}{\sqrt{(1-t^2)(1-xt^2)}} \qquad \text{and} \qquad E(x) = \int_0^1 \mathrm{d}t \sqrt{\frac{1-xt^2}{1-t^2}}. \tag{11}$$

In this case, the normal-frequency mode can be expressed as

$$\omega_{0,\|} = \omega_p \sqrt{1 - 2y\left(\frac{L_n}{R}\right)}, \tag{12}$$

where $\omega_p = (n_0 e^2/\varepsilon_0 m_e)^{1/2}$, and the electron density is $n_0 = N_e/\pi R^2 L_n$. In the thin-disk limit $(x = L_n/R \ll 1)$, it is obtained [17]

$$\omega_{0,\|}^{\text{disk}} \simeq \omega_p \left\{1 - \frac{L_n}{4\pi R}\left[6\ln 2 - 1 - 2\ln\left(\frac{L_n}{R}\right)\right]\right\}, \qquad L_n/R \ll 1, \tag{13}$$

which approaches the ω_p in the limit $L_n/R \to 0$; see details in Figure 4.

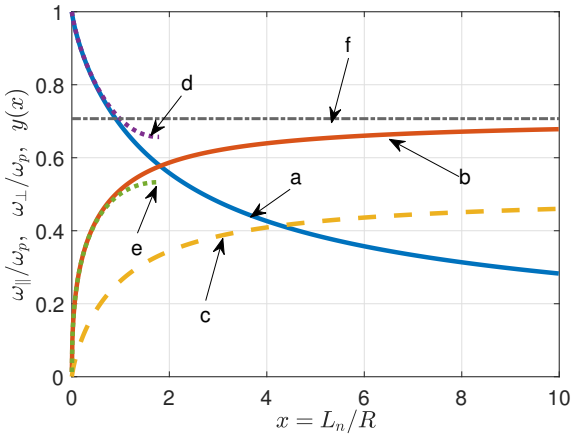


Figure 4. Dependencies $\omega_\|/\omega_p$ (13) (a) and $\omega_\perp/\omega_p$ (14) (b) on parameter $x = L_n/R$. Dotted lines ((d) and (e)) show the approximate solutions. It is seen that such an approximation is correct only for $L_n/R < 0.9$. For $x \approx 1.75$, the values of $\omega_\|$ and $\omega_\perp$ are close. The yellow dashed line (c) displays the function $y(x)$ from Equation (9), and the black line (f) displays the asymptotic value $1/\sqrt{2}$ of the normalized surface plasmon frequency for $x \gg 1$.

The case of the transverse plasmonic mode of the TE type ($\alpha = \perp$) can be studied in a similar way as above for the longitudinal mode, which results in the following expression for the transverse mode frequency:

$$\omega_{0,\perp} = \omega_p \sqrt{y(x)}, \quad x \equiv L_n/R. \tag{14}$$

In Figure 4 the solid lines show dependencies of $\omega_{\parallel}/\omega_p$ and $\omega_{\perp}/\omega_p$ on $x = L_n/R$ in the interval $[0, 10]$, while the dotted lines show the corresponding approximate solutions. It is seen that the latter approximations are valid for $L_n/R < 0.9$. In addition, it is seen in Figure 4 that the contribution of $E_{\perp}$ is small at $|x| \ll 1$; hence, the contribution of $E_{\perp}$ becomes comparable with $E_{\parallel}$ at $x \approx 2$, which corresponds to a cylindrical particle, rather than the ring studied here.

4. Resonant Emission of Nanoemitters in the System with NRs

In this section, we study the dynamics of the system of Equations (1)–(4), which combines Maxwell's equations for the PP field with the semiclassical approximation for the optical field emission from the NEs. We apply the FDTD technique to calculate the field in the NR lattice with the incorporated NEs. Our system (see Figure 1) contains the periodic lattice of conducting NRs (of the size 7×7) with embedded NEs emitting the optical field. PPs are excited in the NRs and interact with the NEs. In Figure 1, the NEs are connected by dashed blue lines that correspond to the TSP optimized path (when, as mentioned in Section 2, a traveling photon passes each NE, without visiting the same NE twice [10]). We use an advanced technique where the standard FDTD approach is extended by calculating the dynamics of the semiclassical polarization system (see Equation (2)) coupled to the population dynamics in the four-level laser NEs (Equations (3) and (4)), at each time step; see further details in Ref. [22]. In this study, numerical calculations were performed by means of the standard FDTD technique [16]. Also, the open source package `fdtd` was used, which allowed us to include the necessary extensions related to the modeling of the Drude frequency dispersion in NRs; see [23] for further details. To simulate the field dynamics in the hybrid system with open boundaries, the standard perfectly matched layer (PML) boundary conditions are applied at boundaries of the FDTD grid, to avoid the reflection of electromagnetic waves from the boundary [16]. On the adopted scale, the typical NE size is orders of magnitude smaller than the typical NR size, and therefore the NEs are approximated here by the point-like sources. In our simulations we dealt with the general 3D vector electromagnetic fields **E** and **H** in the general form. The simulations demonstrate that, in the present system, TM electromagnetic waves with components $[E_z, H_x, H_y]$ are mainly generated. This conclusion agrees with the theory in Ref. [17], where it was shown that, in the case of nano-objects in the disk limit ($L_n/R \ll 1$), the main contribution yields the E_z (alias $E_{\parallel}$) longitudinal field, while the transverse field is conspicuous at $L_n/R \approx 1$ [17]. Thus, in the disk limit one can obtain $\omega_{0,\parallel} \simeq \omega_p$, which approaches the ω_p value in the considered limit of $L_n/R \to 0$. For the TE mode, the transverse frequency is estimated as $\omega_{0,\perp}/\omega_p \sim \sqrt{L_n/R}$, which is small in the present case, $L_n/R \to 0$. To make the following figures clear, only the $|E_z|$ field components are displayed in them. The dynamics of the present hybrid system significantly depend on the frequency ω_p of the dispersive NRs in the terahertz range. Therefore, in the following we focus on two cases, viz., $\omega_p = 2.3$ THz and $\omega_p = 2.3 \times 10^{-2}$ THz, in which ω_p differs by two orders of magnitude.

Figure 5 displays the dynamics produced by the numerical solution of Equations (1)–(5) for the 7×7 NR lattice for two different NE plasma frequencies, $\omega_p = 2.3 \times 10^{-2}$ and 2.3 THz. Figure 5a,b display the dynamics of the populations of the resonant emission NE

levels $N_{1,2}$; see Equation (4) (the evolution of $N_{0,3}$ is not displayed here). Figure 5c,d show the evolution of the average quantum polarization $|\mathbf{P}|$ and photocurrent $i_{\rm ph} = \partial|\mathbf{P}|/\partial t$. Further, Figure 5e,f show details of the average NR current $\langle J\rangle$ (15). We observe that in both cases the evolution of $\langle J\rangle$ drastically differs for different values of ω_p. At $\omega_p = 2.3$ THz, the amplitude of $\langle J\rangle$ is significantly larger than at $\omega_p = 0.023$ THz. It is seen that, at large times $t > 60$, the evolution is chaotic, weakly depending on details of the NE distribution. Such a behavior of $N_{1,2}$, displayed in Figure 5, indicates the onset of the effective coupling of the PP and NE subsystems, which significantly depends on ω_p.

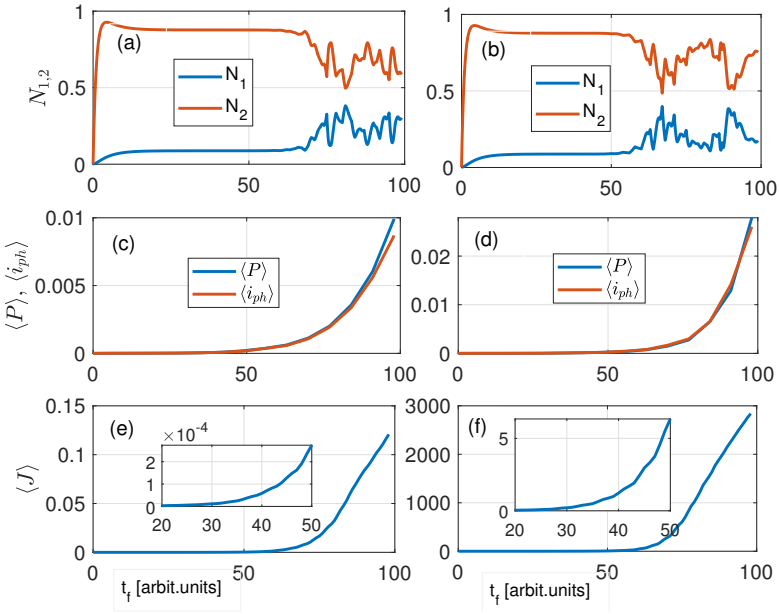


Figure 5. The temporal dynamics produced by the numerical solution of the system (1)–(5) for the 7×7 NR lattice with two plasma frequencies: $\omega_p = 2.3 \times 10^{-2}$ THz (**left**) and 2.3 THz (**right**): the dynamics of populations N_1 (**a**) and N_2 (**b**) of the NE lasing levels, respectively (see Equation (4)); the dynamics of populations $N_{0,3}$ (see Equation (3)) are not displayed here; the average quantum polarization $|\mathbf{P}|$ (**c**) and photocurrent $i_{\rm ph} = \partial|\mathbf{P}|/\partial t$ (**d**); the average current $\langle J\rangle$ (15) in NRs for $\omega_p < \omega_c$ (**e**) and $\omega_p > \omega_c$ (**f**), where $\omega_c \approx 4.93 \times 10^{11}$ HZ is the critical frequency, exhibit drastical difference.

Figure 6 exhibits details of the population dynamics for $N_{0,1,2,3}$ of the four-level NE at $t_f > 20$, when the system commences the transit to the nonlinear regime. From Figure 6, it can be seen that, at $t_f > 58$, the stationary values of the population levels become unstable and convert into a nonlinear oscillatory regime. To define the time when the instability commences, we studied the behavior of the Lyapunov function E_L. The blue line in Figure 6 represents instability at $t_f > 60$. Further analysis shows that such an instability is regularized by the transition to a regime of nonlinear oscillations between the laser levels N_1 and N_2. To obtain more insight into the dynamics in the hybrid system, it is instructive to consider the N_r-averaged current $\langle J\rangle$ in the NR conductive lattice, which is

$$\langle J\rangle = \langle J(\omega_p)\rangle_{N_r} = (N_r)^{-2}\sqrt{\sum |J_{i,j}|^2}, \tag{15}$$

where $J_{i,j}$ is the current in the NR with coordinates (i,j), and the summation is performed over the entire NR lattice, N_r being the total number of NRs. Figure 7a shows the average PP current $\langle J\rangle$ (15) in the conducting lattice of 7×7 of NRs as a function of the scaled simulation time t_f and plasma frequency ω_p. It is seen that $\langle J\rangle$ emerges from zero at $t_f \approx 55$ and sharply increases at $\omega_p \geq \omega_c \simeq 0.5$ THz, which is a critical value of ω_p, indicating the appearance of the strong coupling between the PP current in the NR lattice and the emission field in the embedded quantum NEs. The critical value ω_c can be extracted from

the data with the help of the standard fitting technique. Figure 7b exhibits the fitting of $\langle J \rangle$ by function

$$\left\langle J\left(\frac{\omega_p}{\omega_c}\right)\right\rangle \propto F(x) = a \cdot [\mathrm{erf}(\log(x/b)) + 1], \quad \text{where } \mathrm{erf}(z_0) = \frac{2}{\sqrt{\pi}} \int_0^{z_0} e^{-z^2} dz. \tag{16}$$

Using the data from our FDTD simulations for $\langle J \rangle$ (blue color in Figure 7b) and Equation (16) allowed us to extract both fitting parameters $a = 0.495$ and $b = 25$ that correspond to $\omega_c = 4.927 \times 10^{11}$ Hz (the red line in Figure 7b) within 95% confidence bounds. The numerical package NumPy 2.2.0 [24] was used for this purpose.

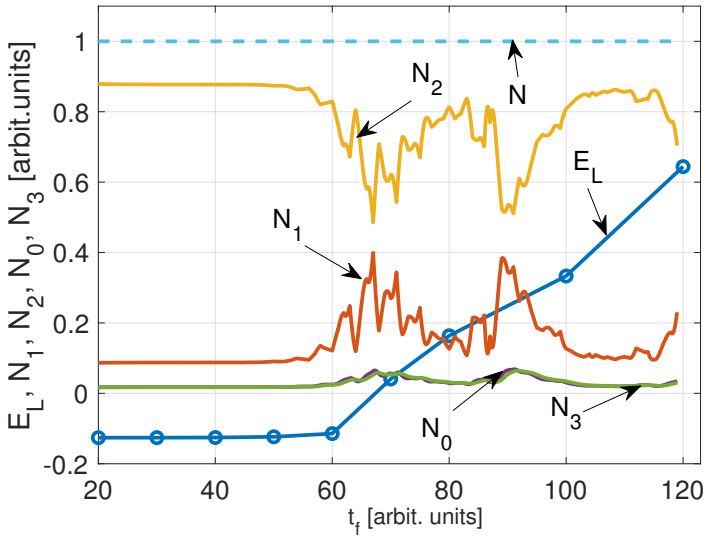


Figure 6. The dynamics of populations $N_{0,1,2,3}$ of the 4-level NE. Red and yellow lines represent, respectively, populations N_1 and N_2 of the lasing levels. The light blue line shows the conservation of $N = N_0 + N_1 + N_2 + N_3$. The blue line exhibits the largest Lyapunov exponent, which changes its value from negative to positive (switching to instability) at dimensionless calculation time $t_f > 60$.

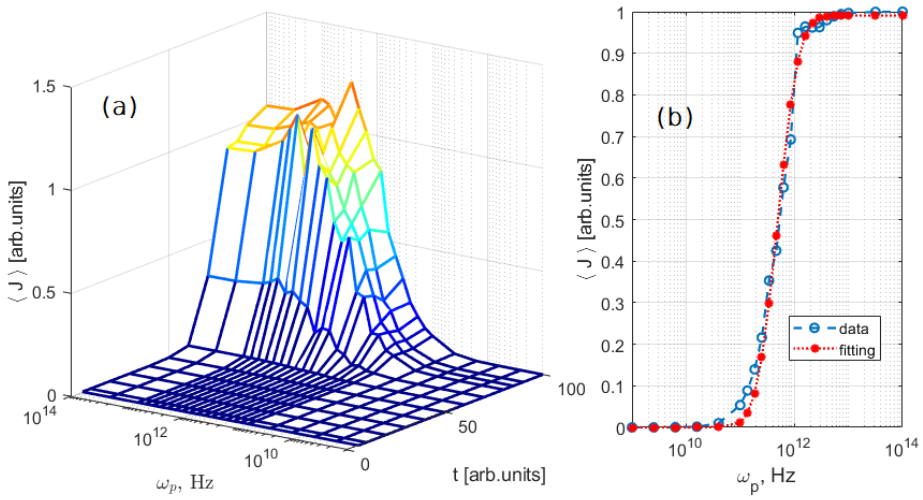


Figure 7. (**a**) The average PP current $\langle J \rangle$ in the conducting lattice of 7×7 NRs as a function time t_f and the NR plasma frequency ω_p. It is seen that $\langle J \rangle$ emerges from zero at $t_f \approx 55$ for $\omega_p \geq \omega_c \simeq 4.93 \times 10^{11}$ Hz. (**b**) The normalized value $\langle J(\omega_p) \rangle$ and its fit by the $\mathrm{err}(\omega_p)$ function, which is found from the FDTD data. See text for details.

To explore details of the nonlinear internal dynamics of the radiating NEs, we calculated the correlation functions (CF) of the z-component of the photocurrent,

$$I_{ij}(t_f, \omega_p) = \left[\mathbf{I}_p \Theta(t_f)\right]_z, \; || \; z\text{-axis of NRs} \tag{17}$$

for different NE pairs (i, j) (see Figure 1) for various values of t_f, where $\Theta(x)$ is the Heaviside step function. The cross-correlation function $\mathrm{CF}(I_i I_j)$ as a function of the time lag τ [25,26] is

$$\mathrm{CF}_{ij}(t_f, \omega_p|\tau) = \mathrm{CF}(I_i I_j) = \frac{1}{s_i s_j N_s} \sum_{m=1}^{N_s} \Delta I_i(t_m) \Delta I_j(t_m + \tau), \tag{18}$$

where $\Delta I_i(t_m) = I_i(t_m) - \overline{I}_i$, $\overline{I}_i$ is the mean value, and $s_k^2 = 1/(N_s - 1) \sum_{m=1}^{N_s} \Delta I_k(t_m)^2$.

Figure 8 displays the cross-correlation function of the photocurrents CF_{12} (18) for different times t_f at fixed $\omega_p = 2.3$ THz for the FDTD solutions of the system of Equations (1)–(5). From Figure 8, it is seen that, at small $t_f \leq 40$, CF_{12} rapidly decays, but at $t_f \geq 60$ the correlations significantly increase, due to the establishment of collective synchronization between all the NEs through the laser emission.

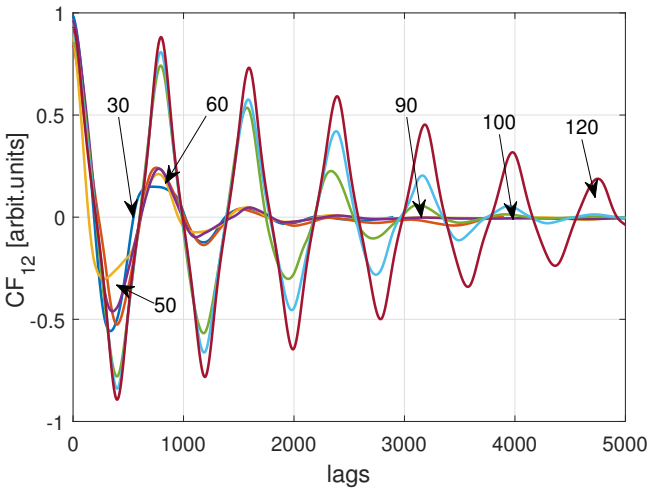


Figure 8. The cross-correlation function of the photocurrent CF_{12} for the NEs with numbers 1 and 2 for different times t_f and $\omega_p = 2.3$ THz, produced by the FDTD solutions of the system (1)–(5). It is seen that, at small times, $t_f \leq 40$, CF_{12} rapidly decays, but at larger times, $t_f \geq 60$, the level of the NE cross-correlations in the lattice significantly increases.

It is instructive to study the dependence of the correlation on the NR plasma frequency ω_p. Such a study turns out to be more informative when comparing the residuals of the cross-correlation functions of the NE photocurrents,

$$\widehat{R}(t_f, \omega_p) = R_{ij,km}(t_f, \omega_p) = \sum_l \left[\mathrm{CF}_{ij}(t_f, \omega_p|\tau_l) - \mathrm{CF}_{km}(t_f, \omega_p|\tau_l)\right]^2, \tag{19}$$

as a function of ω_p. Figure 9 shows a family of such dependencies $R(\omega_p)$ for different times t_f and different NE pairs (i, j) and (k, m).

In Figure 9, the black dashed lines indicate the transition region in terms of the average current $\langle J \rangle$ (15). Figure 9 demonstrates the appearance, in the transition region, of a zone similar to chimera states (shown by isolated circles). In this range, even a small variation in ω_p leads to a significant change in the magnitude of the cross-correlations of the NE pairs. This findingindicates that, for the coupled PPs and NEs, the dynamics of the optical

field in the quantum NE subsystem essentially depends on ω_p, which is a parameter of the classical NR subsystem. Further, the black dashed lines allow one to compare the classical PP dynamics in the NRs with the dynamics of the quantum NE subsystem (photocurrent) in the critical region, 100 GHz $< \omega_p <$ 1 THz. From Figure 9 it is seen that, outside the critical region, the branches of the $\widehat{R}(t_f, \omega_p)$ curves are smooth, which makes it possible to connect them by solid lines (to guide the eye). This observation implies a weak coupling between the PP and NE subsystems in this range, where the conducting NR is actually a dielectric (roughly, at $\omega_p \lesssim 10$ GHz). Note also that, as seen from Figure 9, in this configuration $\widehat{R}(t_f, \omega_p)$ remains small for the NE pairs $(0,1)$–$(0,2)$ and $(0,2)$–$(1,2)$, and therefore those pairs are insignificant. Thus, it is seen in Figure 9a that, at $t_f = 20$, the curve $\widehat{R}(t_f, \omega_p)$ has a characteristic smooth shape, the details of which depend on t_f. At $t_f = 20$, as ω_p is approaching the characteristic value ω_c from below, the $\widehat{R}(t_f, \omega_p)$ remains a smooth function of ω_p with a local minimum. At $t_f = 30$ (see Figure 9b), this minimum deepens, and the dependence $\widehat{R}(t_f, \omega_p)$ loses its smoothness in the critical region. In this zone, due to their chaotic positions, the connection of adjacent points loses its meaning, and in Figure 9 they appear as a cloud of isolated points. Our calculations show that, in the critical region, the standard deviation [27] of the value of $\widehat{R}(t_f, \omega_p)$ is significantly higher than outside of it. As can be seen from Figure 9c–f, with the further increase in τ_f towards $t_f > 50$, the apparently chaotic set of points in the critical region cease changing. Outside the critical region the dependencies $\widehat{R}(\omega_p)$ are found to be smooth.

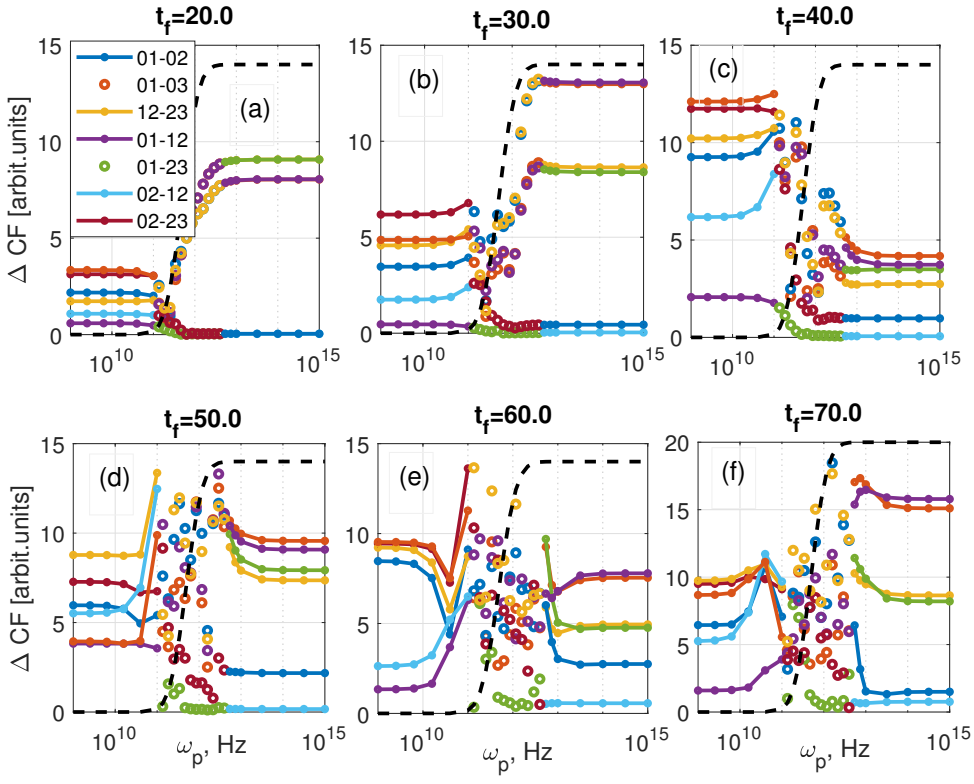


Figure 9. The $\widehat{R}(t_f, \omega_p)$ norm (19) of the residual of the cross-correlations of the photocurrents for different NE pairs (i,j) and (k,m) as a function of ω_p, for different t_f: (**a**) 20, (**b**) 30, (**c**) 40, (**d**) 50, (**e**) 60, and (**f**) 70. The color lines correspond to (i,j)–(k,l) NE pairs as indicated. The black line indicates the transition region (see Figure 7b) of average current $\langle J \rangle$ (15) in the NR lattice. Equation (15)]. The chimera-like states (isolated points) are observed in the transition area.

5. Discussion

In this paper, we have addressed the coupling of the NEs (nanoemitters) and PPs (plasma polaritons) in the hybrid system, built as the periodic lattice of conducting NRs (nanorings) with embedded NEs, through the common optical field. The structure of the field significantly depends on the NR plasma frequency ω_p. At the critical value of ω_p, the phase transition occurs in the system, leading to the sharp increase in the average NR current. In this case, the PP field disturbs the internal degrees of freedom of the quantum NEs, inducing the cross-correlation of the photocurrents in all NEs, the correlation magnitude significantly depending on ω_p. The instability of the NE resonant emission leads to the appearance of non-smooth (chimera- or chaos-like) features. In this regime, a small enough variation in ω_p leads to a significant change in the magnitude of the cross-correlations of NE pairs. Figure 9 exhibits a possibility of the coexistence of the localized synchronized and desynchronized cross-correlations of NEs embedded in the lattice of identical NRs, which results in the formatting of inhomogeneous states in the hybrid system. Similar (quasi-chaotic) behavior is known in Kuramoto systems of coupled oscillators [13,28]. Patterns featuring this behavior are unstable and are identified as chimeras [29]. It is instructive to study the evolution of such irregular states. Figure 3 shows a typical size of the field regions surrounding PPs in the NR lattice. Initially these areas are well separated and expand with the increase in time t_f up to $t_f \approx 80$, when the expanding areas overlap. The latter signifies that initially desynchronized (due to the spontaneous emission) NEs develop synchronization (induced emission) at $t_f \approx 80$. Following the commonly adopted (scalar) metric S of a curve for non-smoothness [30], we define the non-smoothness S for our case (the instability of cross-correlations of NE pairs as

$$S(t_f) = \int \left(\frac{d^2 f(t_f, \omega)}{d\omega^2} \right)^2 d\omega, \quad f(t_f, \omega_p) = \widehat{R}(t_f, \omega_p), \tag{20}$$

over the curve's domain ω_p; see Figure 9a–f. A lower value of $S(t_f)$ distictly indicates a smoother curve. (The natural cubic spline minimizes the L_2 norm of the second derivative among all C_2, the function being continuous with its first and second derivatives, interpolating functions passing through the given points, see [29,30]).

In the system under study, the critical behavior occurs in nonlinear quantum NEs in the respective range of values of the plasma frequency ω_p in the NR lattice.

As Figure 6 shows, the maximum Lyapunov exponent takes positive values in the critical region, indicating unstable dynamics of the system. Figure 3 demonstrates, as said above, that the effective coupling of the NE oscillators to the PPs in the periodic NR lattice leads to the dependence of the evolution of the corresponding chimera-like states on the NR parameter ω_p. Figure 10 exhibits the dynamics of maximum value of the non-smoothness parameter, $S(t_f)_{\max} = \max(S_{t_f})$ (see Equation (20)) of the chimera-like states (red points), displayed in Figure 9a–e, for all the NE pairs, as a function of time t_f in the area of $\omega \approx \omega_c$ (see Figure 9). $S_{\max}$ attains the largest value at $t_f \approx 76$, indicating a highly non-smooth structure, as expected for chimera states [12,13]. Ref. [31] reported an advanced technology based on hybrid nanomaterials, such as sandwiched graphene oxide, and self-assembly of carbon nanotubes (CNT) into CNT rings. The latter, in particular, allows adjusting ω_p of CNT rings to the desired range of ω_p.

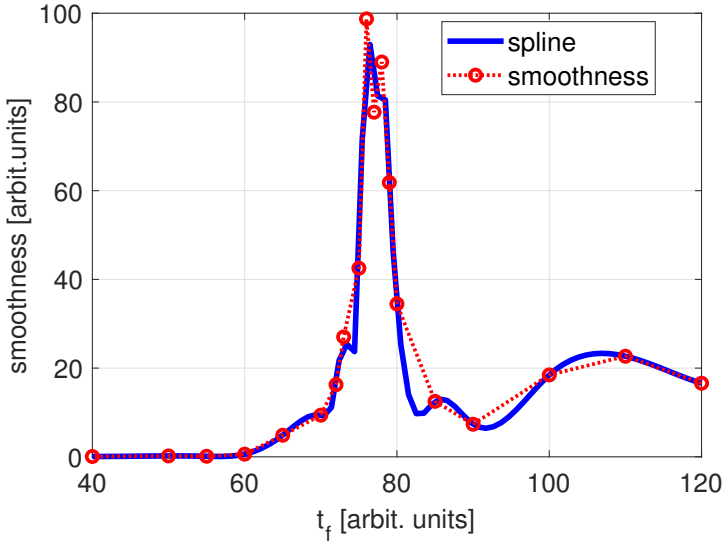


Figure 10. The maximum value of the non-smoothness parameter, $S(t_f)_{\max} = \max(S_{t_f})$ (see Equation (20)) of the chimera-like states (red points), displayed in Figure 9a–e, for all the NE pairs, as a function of time t_f in the area of $\omega \approx \omega_c$ (see Figure 9). $S_{\max}$ attains the largest value at $t_f \approx 76$, indicating a highly non-smooth structure, as expected for chimera states [12,13].

6. Conclusions

We have studied a hybrid system, built as an NR lattice carrying PPs with nonlinear quantum NEs embedded in the lattice. It is found that the strong coupling between the PPs and NEs, mediated by the optical field, leads to the significant cross-correlation between NE pairs, so that the NE dynamics demonstrate essential dependence on the NR plasma frequency ω_p. However, at larger $\omega_p \geq \omega_c$ a transition occurs to the state in which the PP field produces a significant contribution to the radiation field, which perturbs the dynamics of NEs, leading to a change in their cross-correlations. In such a system, the NEs are coupled to the PP field in the NRs, which contributes to the NEs' optical field. As ω_p increases, the PP field attains a significant amplitude, which causes a strong coupling between PPs and NEs and reorientation of the field direction parallel to the PP field in the NRs. This finding leads to a significant dependence of the shape of the cross-correlation of photocurrents in NE pairs on the plasma frequency ω_p of the NRs coupled to the NEs.

Author Contributions: Conceptualization, B.A.M. and G.B.; methodology, B.A.M., G.B. and G.M.-Á.; software, G.B. and G.M.-Á.; validation, B.A.M., G.B., G.M.-Á. and Y.K.; formal analysis, B.A.M., G.B., G.M.-Á. and Y.K.; investigation, B.A.M., G.B. and G.M.-Á.; writing—original draft preparation, B.A.M., G.B. and G.M.-Á.; writing—review and editing, B.A.M., G.B., G.M.-Á. and Y.K.; visualization, G.B. and G.M.-Á.; supervision, B.A.M. and G.B. All authors have read and agreed to the published version of the manuscript.

Funding: G.M.-Á. acknowledges a fellowship provided by SECIHTI-México.

Data Availability Statement: The data that support the main findings of this study are available in a publicly accessible repository at the link https://drive.google.com/drive/folders/1w-uolJkl5X0rIBNLozCk85OTC-BbxBl_?usp=sharing (accessed on 25 October 2025) and from the corresponding author upon reasonable request.

Conflicts of Interest: The authors declare no conflicts of interest.

References

1. Ba, K.; Wang, J. Advances in solution-processed quantum dots based hybrid structures for infrared photodetector. *Mater. Today* **2022**, *58*, 119–134. [CrossRef]
2. Perera, A. Homo- and heterojunction interfacial workfunction internal photo-emission detectors from UV to IR. In *Advances in Infrared Photodetectors*; Gunapala, S.D., Rhiger, D.R., Jagadish, C., Eds.; Academic Press/Elsevier Inc.: San Diego, CA, USA, 2011; pp. 243–302. [CrossRef]
3. Jain, R.K.; Hoffman, A.J.; Jepsen, P.U.; Liu, P.Q.; Turchinovich, D.; Vitiello, M.S. Mid-infrared, long-wave infrared, and terahertz photonics: Introduction. *Opt. Express* **2020**, *28*, 14169–14175. [CrossRef]
4. Dai, T.; Guo, S.; Duan, X.; Dou, R.; Zhang, Q. High efficiency single-longitudinal-mode resonantly-pumped Ho:GdTaO4 laser at 2068nm. *Opt. Express* **2019**, *27*, 34204–34210. [CrossRef] [PubMed]
5. Ryzhii, V.; Ryzhii, M.; Mitin, V.; Shur, M.S.; Otsuji, T. Far-infrared photodetectors based on graphene/black-AsP heterostructures. *Opt. Express* **2020**, *28*, 2480–2498. [CrossRef] [PubMed]
6. Arrazola, I.; Hillenbrand, R.; Nikitin, A.Y. Plasmons in graphene on uniaxial substrates. *Appl. Phys. Lett.* **2014**, *104*, 011111. [CrossRef]
7. Guo, J.; Black, K.; Hu, J.; Singh, M. Study of plasmonics in hybrids made from a quantum emitter and double metallic nanoshell dimer. *J. Phys. Condens. Matter* **2018**, *30*, 185301. [CrossRef]
8. Habisreutinger, S.N.; Blackburn, J.L. Carbon nanotubes in high-performance perovskite photovoltaics and other emerging optoelectronic applications. *J. Appl. Phys.* **2021**, *129*, 010903. [CrossRef]
9. Burlak, G.; Medina-Angel, G.; Calderon-Segura, Y. Plasmon-mediated dynamics and lasing of nanoemitters enhanced by dispersing nanorings. *J. Chem. Phys.* **2024**, *161*, 034110. [CrossRef]
10. Burlak, G.; de Anda, A.D.; Malomed, B.A.; Martinez-Sánchez, E.; Medina-Ángel, G.; Morales-Nava, R.; Martínez-Ocampo, J.; de Anda-Reyes, M.; Romero-López, A. Critical properties of the optical field localization in a three-dimensional percolating system: Theory and experiment. *Chaos Solitons Fractals* **2023**, *173*, 113734. [CrossRef]
11. Siegman, A.E. *Lasers*; University Science Books: Mill Valley, CA, USA, 1986. Available online: https://www.scribd.com/document/545876011/Siegman-Lasers-1986 (accessed on 3 January 2026).
12. Abrams, D.M.; Strogatz, S.H. Chimera states for coupled oscillators. *Phys. Rev. Lett.* **2004**, *93*, 174102. [CrossRef]
13. Davidsen, J.; Maistrenko, Y.; Showalter, K. Introduction to Focus Issue: Chimera states: From theory and experiments to technology and living systems. *Chaos Interdiscip. J. Nonlinear Sci.* **2024**, *34*, 120402. [CrossRef] [PubMed]
14. Burlak, G.; Rubo, Y.G. Mirrorless lasing from light emitters in percolating clusters. *Phys. Rev. A* **2015**, *92*, 013812. [CrossRef]
15. Jiang, X.; Soukoulis, C.M. Time dependent theory for random lasers. *Phys. Rev. Lett.* **2000**, *85*, 70–73. [CrossRef] [PubMed]
16. Taflove, A.; Hagness, S.C. *Computational Electrodynamics: The Finite-Difference Time-Domain Method*; Artech House: Norwood, MA, USA, 2005.
17. Downing, C.A.; Weick, G. Plasmonic modes in cylindrical nanoparticles and dimers. *Proc. R. Soc. A Math. Phys. Engin. Sci.* **2020**, *476*, 20200530. [CrossRef]
18. Cao, H.; Zhao, Y.G.; Ho, S.T.; Seelig, E.W.; Wang, Q.H.; Chang, R.P.H. Random laser action in semiconductor powder. *Phys. Rev. Lett.* **1999**, *82*, 2278–2281. [CrossRef]
19. Wang, T.B.; Wen, X.W.; Yin, C.P.; Wang, H.Z. The transmission characteristics of surface plasmon polaritons in ring resonator. *Opt. Express* **2009**, *17*, 24096–24101. [CrossRef]
20. Wolff, I.; Knoppik, N. Microstrip ring resonator and dispersion measurement on microstrip lines. *Electron. Lett.* **1971**, *7*, 779–781. [CrossRef]
21. Abramowitz, M.; Stegun, I.A. (Eds.) *Handbook of Mathematical Functions with Formulas, Graphs, and Mathematical Tables*; Dover Publications, Inc.: Mineola, NY, USA, 1974. Available online: https://store.doverpublications.com/products/9780486612720 (accessed on 3 January 2026).
22. Burlak, G.; Medina-Ángel, G. Extended dynamics and lasing of nanoemitters enhanced by dispersing single-walled carbon nanotubes. *J. Quant. Spectrosc. Radiat. Transf.* **2023**, *296*, 108463. [CrossRef]
23. fdtd. A 3D Electromagnetic FDTD Simulator Written in Python with Optional GPU Support. Available online: https://github.com/flaport/fdtd (accessed on 3 January 2026).
24. NumPy. Available online: https://numpy.org (accessed on 3 January 2026).
25. Williams, C.R.S.; Murphy, T.E.; Roy, R.; Sorrentino, F.; Dahms, T.; Schöll, E. Experimental observations of group synchrony in a system of chaotic optoelectronic oscillators. *Phys. Rev. Lett.* **2013**, *110*, 064104. [CrossRef]
26. Therrien, C.; Tummala, M. *Probability and Random Processes for Electrical and Computer Engineers*; CRC Press/Taylor & Francis Group: Boca Raton, FL, USA, 2018. [CrossRef]
27. Gubner, J.A. *Probability and Random Processes for Electrical and Computer Engineers*; Cambridge University Press: New York, NY, USA, 2006.

28. Lau, H.W.H.; Davidsen, J.; Simon, C. Chimera patterns in conservative Hamiltonian systems and Bose–Einstein condensates of ultracold atoms. *Sci. Rep.* **2023**, *13*, 8590. [CrossRef]
29. Kemeth, F.P.; Haugland, S.W.; Schmidt, L.; Kevrekidis, I.G.; Krischer, K. A classification scheme for chimera states. *Chaos* **2016**, *26*, 094815. [CrossRef]
30. Vettering, W.T.; Teukolsky, S.A.; Press, W.H.; Flannery, B.P. *Numerical Recipes. Example Book (C++)*; Cambridge University Press: New York, NY, USA, 2002.
31. Song, J.; Wang, F.; Yang, X.; Ning, B.; Harp, M.G.; Culp, S.H.; Hu, S.; Huang, P.; Nie, L.; Chen, J.; et al. Gold nanoparticle coated carbon nanotube ring with enhanced Raman scattering and photothermal conversion property for theranostic applications. *J. Am. Chem. Soc. (JACS)* **2016**, *138*, 7005–7015. [CrossRef]

Disclaimer/Publisher's Note: The statements, opinions and data contained in all publications are solely those of the individual author(s) and contributor(s) and not of MDPI and/or the editor(s). MDPI and/or the editor(s) disclaim responsibility for any injury to people or property resulting from any ideas, methods, instructions or products referred to in the content.